NASA-CR-204496

FINAL REPORT : NCC2-5156

Large Scale Turbulent Structures in Supersonic Jets

by

Ram Mohan Rao

and

Thomas S. Lundgren, P.I.

Department of Aerospace Engineering and Mechanics

University of Minnesota, Minneapolis, MN 55455

March 1997

Abstract

Jet noise is a major concern in the design of commercial aircraft. Studies by various researchers[2-5] suggest that aerodynamic noise is a major contributor to jet noise. Some of these studies indicate that most of the aerodynamic jet noise due to turbulent mixing occurs when there is a rapid variation in turbulent structure, i.e. rapidly growing or decaying vortices.

The objective of this research was to simulate a compressible round jet to study the non-linear evolution of vortices and the resulting acoustic radiations. In particular, to understand the effect of turbulence structure on the noise. An ideal technique to study this problem is direct numerical simulations(DNS), because it provides precise control on the initial and boundary conditions that lead to the turbulent structures studied. It also provides complete 3-dimensional time dependent data.

Since the dynamics of a temporally evolving jet are not greatly different from those of a spatially evolving jet, a temporal jet problem was solved, using periodicity in the direction of the jet axis. This enables the application of Fourier spectral methods in the streamwise direction. Physically this means that turbulent structures in the jet are repeated in successive downstream cells instead of being gradually modified downstream into a jet plume.

The DNS jet simulation helps us understand the various turbulent scales and mechanisms of turbulence generation in the evolution of a compressible round jet. These accurate flow solutions will be used in future research to estimate near-field acoustic radiation by computing the total outward flux across a surface and determine how it is related to the evolution of the turbulent solutions. Furthermore, these simulations allow us to investigate the sensitivity of acoustic radiations to inlet/boundary conditions, with possible application to active noise suppresion. In addition, the data generated can be used to compute various turbulence quantities such as mean velocities, turbulent stresses, etc. which will aid in turbulence modeling.

This report will be presented in two chapters. The first chapter describes some work on the linear stability of a supersonic round jet and the implications of this for the jet

noise problem.

The second chapter is an extensive discussion of numerical work using the spectral method which we use to solve the compressible Navier-Stokes equations to study turbulent jet flows. The method uses Fourier expansions in the azimuthal and streamwise direction and a 1-D B-spline basis representation in the radial direction. The B-spline basis is locally supported and this ensures block diagonal matrix equations which can be solved in $O(N)$ steps. This is a modification of a boundary layer code developed by Robert Moser.

A very accurate highly resolved direct numerical simulation (DNS) of a turbulent jet flow is produced.

Chapter 1 : The Linear Stability of a Supersonic Round Jet

Our purpose in doing this stability problem is to provide initial conditions for the nonlinear computations. We want to start with the most unstable disturbance since this is what would be found in the natural problem. This problem has been studied by Tam and Hu(1989) however they didn't present the information which we require. As a result of our computations we have found some new results which have not been previously reported.

The basic stability equation was obtained by linearizing the equations for inviscid compressible flow in cylindrical coordinates, taking small perturbations from an axially symmetric basic state. One can reduce this to a single second order equation for the pressure perturbation, which is expressed in separation of variables form as

$$p = \bar{p}(r) + \hat{p}(r)e^{(i\omega t - ikz - im\theta)}$$

where r is the radial coordinate. The equation for $\hat{p}$ is

$$\frac{d^2\hat{p}}{dr^2} + \Big(\frac{1}{r} + \frac{2kd\bar{u}/dr}{\omega - \bar{u}k} - \frac{1}{\bar{\rho}}\frac{d\bar{\rho}}{dr}\Big)\frac{d\hat{p}}{dr} + \Big(\frac{(\omega - \bar{u}k)^2}{\bar{a}^2} - k^2 - \frac{m^2}{r^2}\Big)\hat{p} = 0$$

where $\bar{u}(r)$ is the prescribed axial velocity profile, $\bar{p}(r)$ and $\bar{\rho}(r)$ the prescribed pressure and density of the base state, and $\bar{a}^2(= \gamma R\bar{T})$ is the square of the sound speed. This equation agrees with Tam and Hu. This equation is to be solved with boundary conditions which require the solution to be bounded at $r = 0$ and to possess only outgoing waves at infinity. It is an eigenvalue problem for complex ω when k and m are given. The flow is unstable if Im$\omega < 0$.

The velocity profile was taken in the same form as in Tam and Hu as a "half-Gaussian" function which is given by

$$\bar{u} = u_j \quad r < h$$

$$\bar{u} = u_j \exp\Big(-\ln 2\big(\frac{r - h}{b}\big)^2\Big) \quad r > h$$

Half – Gaussian jet profile

h = 0.9 r

h + b = r
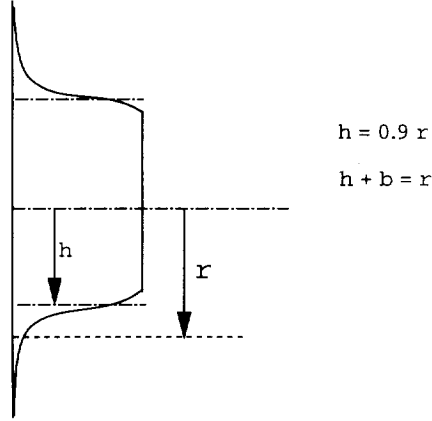
which is sketched here in order to define the parameters b and h. We define the jet radius to be $r_j = b + h$ and all computations were done with $b/r_j = .1, h/r_j = .9$. We have taken the temperature profile to be of a form similar to the velocity

$$\bar{T} = T_j \quad r < h$$

$$\bar{T} = T_\infty + (T_j - T_\infty) \exp\left(-\ln 2\left(\frac{r-h}{b}\right)^2\right) \quad r > h$$

and have taken $\bar{p}(r) = p_\infty$, constant across the jet. Then $\bar{\rho}$ is related to $\bar{T}$ by

$$p_\infty = \bar{\rho} R \bar{T}$$

and

$$\bar{a}^2 = a_\infty^2 \bar{T}/T_\infty.$$

Sometimes in problems like this the temperature is related to the velocity profile by the Crocco-Buseman formula. But this is a viscous dominated profile which results when the Prandtl number is unity, and it doesnt make a lot of sense for high Reynolds number flows such as this. In all the work done by us so far we have taken $T_j = T_\infty$ so the temperature is constant across the jet. This could be called a "warm " jet : the stagnation temperature has to be high to compensate for expansion cooling.

We have solved this eigenvalue problem by a method described in a book by Betchov and Criminale. We integrate inward from a large radius, using an asymptotic formula to identify outgoing waves, and we integrate outward from the origin. Where the two

4

computations meet we must have $\hat{p}$ and $d\hat{p}/dr$ continuous. This does not occur unless ω has the proper value. We iterate on ω using a Newton-Raphson procedure until our continuity requirement is attained. The biggest problem was that the procedure doesn't converge unless one starts near the proper value. This means that is was necessary to change parameters by small increments, starting from a known result.

Results have been obtained for jet Mach numbers of $M_j = 2$ and 2.5. The result for $M_j = 2$ is shown in a figure at the end of this section. Here we present curves of growth rate versus k for a number of values of m (the azimuthal wavenumber). What is observed is that the maximum growth rate for given m increases as m increases, reaching a maximum at $m = 4$ and then it decreases again as m becomes greater than 4. This means that of all azimuthal wavenumbers the most unstable wave is $m = 4$ (and also $m = -4$ since only m^2 occurs in the equation). For $M_j = 2.5$ the maximum is at $m = \pm 5$.

A wave $\exp(-ikz - im\theta)$ is interpreted as a helical wave on the surface of the jet, with the wave making an angle $\tan^{-1}(m/k)$ with the axis of the jet ($m = 0$ is an axial wave). Therefore there are two helical waves of definite angle, one left-handed and one right-handed, which are the most unstable. This is similar to results of Sandham and Reynolds (1990) on the stability of a compressible mixing layer. They find two oblique waves with maximum growth rate which make equal but opposite angles with the flow direction.

There are some implications of this for our proposed nonlinear computation. Sandham and Reynolds (1991) in a second paper find a single oblique unstable plane wave rolls up into an oblique vortex. We expect that a single unstable helical wave will roll up into a helical vortex. Since our helical waves propagate downstream with a speed which is about .66 times the jet speed, we expect a similar speed for the helical vortex. A propagating helix will appear like a rotating helix–as a barber pole does. This is an interesting result because there are observed jet modes, called spinning modes, where the noise field rotates around the jet axis, so that to an observer on one side the sound appears to have a time periodicity(Wesley and Woolley, 1975).

Sandham and Reynolds found that the angle of the most unstable oblique wave de-

5

pends on the convective Mach number in such a way that $M_c \cos \alpha \simeq .6$, so that the component of the Mach number perpendicular to the wave stays constant (and subsonic). We find approximately the same result for the helical waves, based on only two Mach numbers. In the Sandham-Reynolds nonlinear computations they find that because the normal Mach number is subsonic the oblique vortex forms without shock waves (unlike their strictly two-dimensional computations which do have shocks). This is possibly very significant for our proposed computations. It means that helical vortices could form without shocks. This is important when we use the B-spline/spectral method because any shocks will have to be resolved by viscosity alone which could restrict our Reynolds number range.
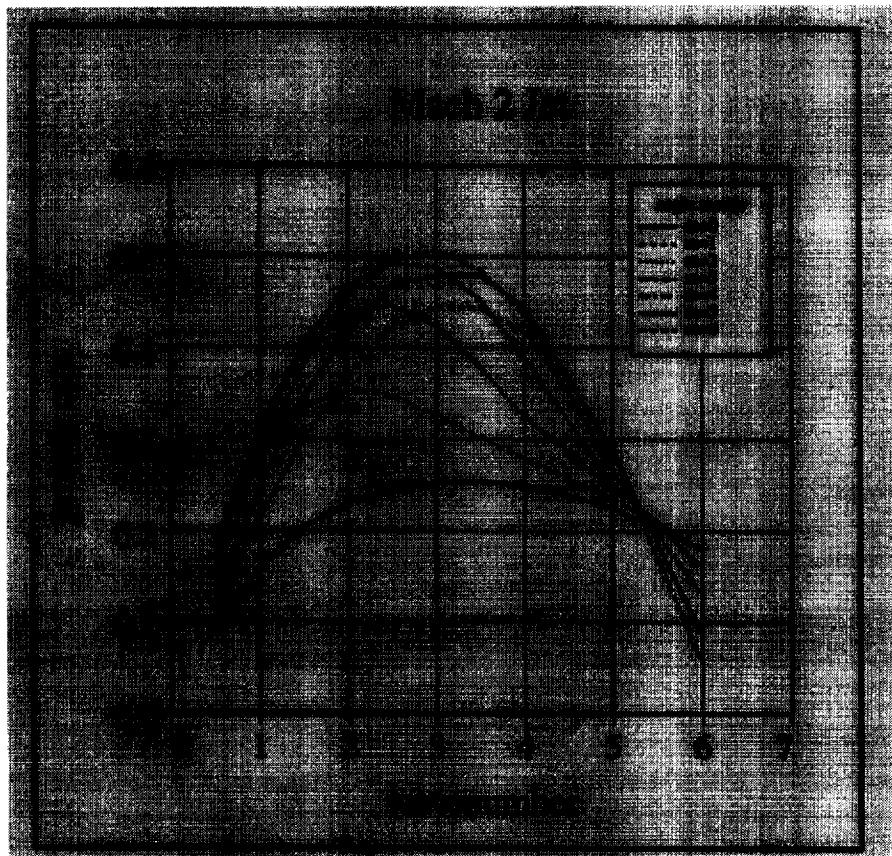
References for Chapter 1

[1] Sandham, N. D., & Reynolds, W. C., " Compressible mixing layer: linear theory and direct simulation ", AIAA *Journal*, **28**, 1990, pp. 618–624.

[2] Sandham, N. D., & Reynolds, W. C., " Three-dimensional simulations of large eddies in the compressible mixing layer ", *J. Fluid Mech.*, **224**, 1991, pp. 133–158.

[3] Tam, C. K. W., and Hu, F. Q., " On the three families of instability waves of high speed jets ", *J. Fluid Mech.* **201**, 1989, pp. 447–483.

[4] Westley, R., and Woolley, J. H., " Sound pressures of a choked jet oscillating in the spinning mode ", Presented as Paper 75-479 at the AIAA 2nd Aero-Acoustics Conference, Hampton, Va. 1975.

Chapter 2 : Direct Numerical Simulation of Unsteady, Compressible Round Jets

Introduction

Jet noise is a major concern in the design of a supersonic transport (SST) aircraft. Studies by various researchers[2-4] lead to aerodynamic noise as a major contributor to jet noise. Some of these studies indicate that most of the aerodynamic jet noise due to turbulent mixing occurs when there is a rapid variation in turbulent structure, i.e. rapidly growing or decaying vortices.

The object of this work is to obtain highly accurate flow solutions of a turbulent round jet. These solutions are expected to help understand the various turbulent scales and mechanisms of turbulence generation in the evolution of a compressible round jet. We hope to use these accurate flow solutions to estimate acoustic radiation in the near-field region. Also the data generated can be used to compute various turbulence quantities such as mean velocities, turbulent stresses, etc. which may aid in turbulence modeling.

We simulate a compressible round jet by using Fourier expansions in the azimuthal and streamwise direction and a 1-D B-spline basis representation in the radial direction. This is an efficient and accurate way to separate out the θ and z variables, leaving partial differential equations(PDEs) depending on r and t only. By using a 1-D B-spline basis and a Galerkin approximation we can reduce this set of PDEs to ordinary differential equations(ODEs) in time. This is solved by a 3rd order Runge-Kutta time marching scheme. The present study uses a spectral method developed by Moser et al.[7]

We consider the temporal jet problem for two reasons: one since this configuration allows for the application of highly accurate spectral methods and the other because the dynamics of the temporal jet is not greatly different from that of a spatially evolving jet. The spectral accuracy helps capture smaller turbulent scales.

Governing Equations

The compressible Navier-Stokes equations written in cylindrical coordinates in non-dimensional form are,

$$\frac{\partial \sigma}{\partial t} = \sigma^2 \left(\frac{1}{r}\frac{\partial (r m_r)}{\partial r} + \frac{1}{r}\frac{\partial m_\theta}{\partial \theta} + \frac{\partial m_z}{\partial z} \right) \qquad (1)$$

$$\frac{\partial m_r}{\partial t} + \frac{\sigma}{r}(m_r^2 - m_\theta^2) = -\frac{\partial \sigma m_r m_k}{\partial x_k} - \frac{\partial P}{\partial r} + \frac{1}{Re}\left(\frac{\partial \tau_{rk}}{\partial x_k} + \frac{\tau_{rr} - \tau_{\theta\theta}}{r} \right)$$

$$\frac{\partial m_\theta}{\partial t} + \frac{2\sigma}{r}m_r m_\theta = -\frac{\partial \sigma m_\theta m_k}{\partial x_k} - \frac{1}{r}\frac{\partial P}{\partial \theta} + \frac{1}{Re}\left(\frac{\partial \tau_{\theta k}}{\partial x_k} + 2\frac{\tau_{\theta r}}{r} \right) \qquad (2)$$

$$\frac{\partial m_z}{\partial t} + \frac{\sigma}{r}m_r m_z = -\frac{\partial \sigma m_z m_k}{\partial x_k} - \frac{\partial P}{\partial z} + \frac{1}{Re}\left(\frac{\partial \tau_{zk}}{\partial x_k} + \frac{\tau_{zr}}{r} \right)$$

$$\frac{\partial P}{\partial t} + \nabla \cdot P\vec{u} = -(\gamma - 1)P\nabla \cdot \vec{u} + \frac{1}{Re\,Pr}\nabla \cdot \vec{q} + \frac{(\gamma - 1)}{Re}\Phi \qquad (3)$$

where,

$$\frac{\partial}{\partial x_1} = \frac{\partial}{\partial r}, \quad \frac{\partial}{\partial x_2} = \frac{1}{r}\frac{\partial}{\partial \theta}, \quad \frac{\partial}{\partial x_3} = \frac{\partial}{\partial z}$$

$$\sigma = \frac{1}{\rho}, \quad m_k = \rho\, u_k, \quad Re = \frac{\rho u l}{\mu}, \quad Pr = \frac{\mu C_p}{\kappa}$$

Re, Pr are the Reynolds number and Prandtl number, C_p is the specific heat at constant pressure, and Φ is the viscous dissipation (see Appendix).

B-Spline Representation and Galerkin Formulation

The flow variables are expanded using Fourier sums in the two periodic directions, viz. the azimuthal (θ) and the axial (z) directions. In the non-periodic or radial direction (r) we use 1-Dimensional B-splines as interpolating functions.[1] B-splines have local support and hence lead to sparse block diagonal matrices which can be efficiently stored and solved. Application of boundary conditions is similar in ease to a finite element method (FEM).

B-splines of order n are piecewise polynomials of degree n having $n - 1$ continuous derivatives. Since they have a high degree of continuity derivative quantities (like vorticity) can be smoothly and accurately represented.

They have 1 degree of freedom(d.o.f) per interval unlike finite element(FE) basis which can have as many d.o.f as the order of the polynomial. We use B-spline bases because higher order FE bases may resolve waves of wavelength smaller than twice the interval

length due to the increased d.o.f. But this is beyond the Nyquist cut-off for the interval size and so these increased d.o.f do not improve the resolution (i.e. the smallest accurately represented scale) of the solution only thing that gets better is the accuracy (convergence rate is increased). Higher order B-splines on the other hand not only have better accuracy but also have better resolution of scales per d.o.f.

The Galerkin method using B-splines as basis functions has been used previously by some researchers.[5-7] By using a Galerkin approximation we can approximate the set of PDEs as a set of ODEs in time.

One can use a B-spline basis to represent the desired function $f(x)$ as,

$$f(x) = \sum_{j=-\infty}^{\infty} a_j \, b_j^n(x) \tag{4}$$

where,

$b_j^n(x)$ is a nth order B-spline coefficient, a_j is the value of function at knot j.

Using a Galerkin approximation we can write, (b_k is the weight function)

$$\int b_k \, f(x) dx = \sum_j a_j \int b_j b_k dx \tag{5}$$

Also, the derivative of $f(x)$ can be written as,

$$f'(x) = \sum_j a_j \, b_j'(x) \tag{6}$$

But here the order of the polynomial has reduced by 1 so in order to keep the degree of polynomial the same we approximate the derivative as,

$$f'(x) \approx g(x) \; \Rightarrow \; \sum_j a_j \, b_j'(x) \; \approx \; \sum_j c_j^n \, b_j^n(x) \tag{7}$$

Again the Galerkin approximation is written as,

$$\int b_k \, f'(x) dx \approx \sum_j a_j \int b_j' \, b_k dx \tag{8}$$

10

Any non-linear terms are handled in a similar way, i.e. if

$$h = f \cdot g$$

$$h = \sum_j d_j \, b_j^n(x) \;\approx\; \sum_{j,k} a_j \, c_k \, b_j \, b_k$$

$$\sum_j d_j \int b_j \, b_l \, dx \;\approx\; \sum_{j,k} a_j \, c_k \int b_j \, b_k \, b_l \, dx \tag{9}$$

The matrices (terms with the integral) on the right hand side of equations (5) and (8) are called the mass and derivative matrices respectively. All different combinations of such derivatives and other terms are computed as matrices too. These are calculated only once using a Gaussian quadrature and stored as opposed to a regular finite element (FE) basis where they can be calculated on the fly when required.

Writing the governing equations in the Galerkin form using the B-spline representation yields a number of matrices similar to the mass and derivative matrices, non-linear advection terms yield matrices similar to the non-linear matrix obtained in equation (9).

In Galerkin form the continuity equation can be written for any k_θ and k_z as (k_θ and k_z are wave numbers in the θ and z directions respectively),

$$\frac{\partial}{\partial t} \sigma_i \sum_l \int_R b_i \, b_l \, r dr = \sum_{j,\,k,\,l} \sigma_i \sigma_j \Big(m_{r_k} \int_R \frac{b_i \, b_j \, (r \, b_k)' \, b_l}{r} \, r dr$$
$$+ \frac{\partial}{\partial \theta} m_{\theta_k} \int_R \frac{b_i \, b_j \, b_k \, b_l}{r} \, r dr + \frac{\partial}{\partial z} m_{z_k} \int_R b_i \, b_j \, b_k \, b_l \, r dr \Big) \tag{10}$$

where,

$$\sigma = \sum_k \sigma_k(z,\theta,t) \, b_k(r) \,, \qquad m_\theta = \sum_k m_{\theta_k}(z,\theta,t) \, b_k(r) \,,$$

$$m_r = \sum_k m_{r_k}(z,\theta,t) \, b_k(r) \,, \qquad m_z = \sum_k m_{z_k}(z,\theta,t) \, b_k(r)$$

The Fourier terms ($e^{ik_\theta} e^{ik_z}$) are included in the coefficients of the variables. So $\sigma_k(z,\theta,t) = \sigma_k(t) \sum_{k_\theta} \sum_{k_z} e^{ik_\theta \theta + ik_z z}$ and so on.

Since we are using 1-D B-splines all the integrals are line integrals over the radius. These are computed exactly using Gaussian quadratures (doing integrals exactly takes care

11

of aliasing). The derivatives in the θ and z are taken by Fast Fourier Transforming (FFT) into wave space and multiplying by the appropriate wave numbers k_θ and k_z, and then an inverse FFT is applied to bring it back to physical space.

The momentum and energy equations can be written in a similar manner.
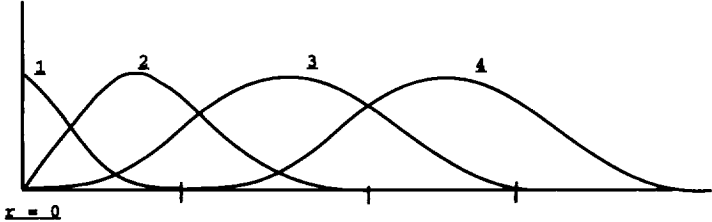
Fig 1   Quadratic B-Splines
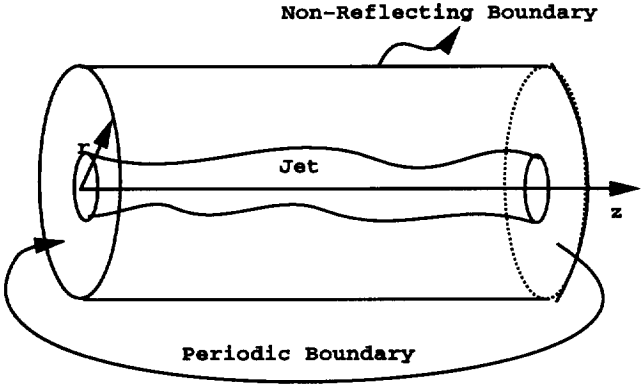
Fig 2   Computational Domain

Numerical Formulation

Writing the flow equations in a manner as discussed above results in a linear system of coupled equations to solve simultaneously at each time step. Since these B-splines (of order n) have local support on $n + 1$ knot(node) intervals (see fig.1) we get a $2n + 1$ block banded matrix system.

$$\mathbf{M} f = R \tag{11}$$

where,

12

$\mathbf{M}$ is the resulting mass matrix, f is the column vector of nodal values we solve for, and R is a column matrix resulting from the RHS of the governing equations.

Time integration is carried out by a 3rd order Runge-Kutta scheme.

Regularity Requirements

In the cylindrical coordinate system the origin $(r = 0)$ is source of concern since some of the functions do not remain analytic as they have a 'r' in the denominator. From a mathematical point of view the flow variables should be single valued and finite. To enforce this the polynomial expansion functions must satisfy some regularity requirements.[8]

The z-component of the velocity should be represented as,

$$u_z(r;\ m,k)\ = a(m,k)\ r^{|m|}\ P_z(r^2;\ m,k)\ e^{i\ m\theta}\ e^{i\ kz},\ m = all\ integers,$$
$$P_z(0;\ m,k) = 1,$$

(12)

where $P_z(r^2;\ m,k)$ is a polynomial in r^2.

Scalars and z-components of all vectors should be represented in a similar manner. The θ and r-components of the vectors are dependent on each other and should be represented as,

$$
\begin{aligned}
u_r(r;\ m,k) &= b(m,k)\ r^{|m|-1}\ P_r(r^2;\ m,k)\ e^{i\ m\theta}\ e^{i\ kz}, \\
u_\theta(r;\ m,k) &= c(m,k)\ r^{|m|-1}\ P_\theta(r^2;\ m,k)\ e^{i\ m\theta}\ e^{i\ kz}, \\
c(m,k) &= ib(m,k)\ \ for\ m\ \geq 1, \\
c(m,k) &= -ib(m,k)\ \ for\ m\ \leq -1, \\
P_r(0;\ m,k) &= P_\theta(0;\ m,k) = 1,
\end{aligned}
$$

(13)

for $m = 0$ $b(m,k)$ and $c(m,k)$ are unrelated.

Enforcing these conditions gives rise to a set of constraint equations which then replace some rows in the mass matrix and suitably modify the RHS vector R.

We can obtain the constraint equations as follows, for a quadratic B-Spline and any scalar u,

$$u(r;\ m,k)\ =\ a(m,k)\ r^{|m|}\ P(r^2;\ m,k)\ e^{i\ m\theta}\ e^{i\ kz}, \ m = all\ integers,$$

Only non-zero derivatives allowed are $|m| + 2j \quad \forall\, j \geq 0$

For quadratic B-splines (see fig.1), at $\underline{r = 0}$, 3 splines have support at the origin. Order of non-zero derivatives for the splines is,

$$Spline\ 1 \Rightarrow 0,\ 1,\ 2$$

$$Spline\ 2 \Rightarrow 1,\ 2$$

$$Spline\ 3 \Rightarrow 2$$

All other splines are zero at $r = 0$.

Consider spline expansions as $\sum_i a_i\ b_i$, where b_i are the spline coefficients. We have in any interval,

$$\sum_i b_i = 1 \Rightarrow b_1 + b_2 + b_3 = 1$$

$$b_1' + b_2' = 0 \Rightarrow b_1' = -b_2'$$

Now consider different values of the azimuthal wave number m,

<u>for $m = 0$</u>

Only non-zero derivatives allowed are $0, 2, \ldots$ even powers, so all odd powered derivatives should be forced to zero. At $r = 0$ splines having non-zero first derivative are splines 1 and 2, so,

$$a_1 b_1' + a_2 b_2' = 0 \tag{14}$$

<u>for $m = 1$</u>

Only non-zero derivatives allowed are $1, 3, \ldots$ odd powers, so all even powered derivatives should be forced to zero. At $r = 0$ splines having non-zero 0th and 2nd derivatives are splines 1 and splines 1, 2, and 3 respectively, giving constraints,

$$a_1 = 0,\ and$$

$$a_2 b_2'' + a_3 b_3'' = 0 \tag{15}$$

14

Similarly,

for $m = 2$

Only non-zero derivatives allowed are 2, 4, ... even powers, giving

$$a_1 = 0, \quad a_2 = 0 \tag{16}$$

and

for $m = 3$

Only non-zero derivatives allowed are 3, 5, ... odd powers, so

$$a_1 = a_2 = a_3 = 0 \tag{17}$$

or, all splines should be zero. For all other values of m we get the same result as (17). Now equations (14-17) are the **constraint equations** which will replace the appropriate rows in the matrix $\mathbf{M}$ and vector R.

Before replacing rows which actually contain the physics of the flow care has to be taken to see that no information is lost. So, we need to take a linear combination of those rows to be replaced and add them to the remaining rows in a particular manner. For this the null space of the constraint equations has to be computed and the eigenvectors of this space are to be used for the linear combination. This is done as shown below.

for $opol = 7$ and $m = 1$

The first set of rows in the mass matrix are written as,

$$\mathbf{m}' = \begin{pmatrix} 1 & 0 & 0 & 0 & 0 & 0 & 0 \\ * & * & * & * & * & * & * \\ 0 & b_2^2 & b_3^2 & 0 & 0 & 0 & 0 \\ * & * & * & * & * & * & * \\ 0 & b_2^4 & b_3^4 & b_4^4 & b_5^4 & 0 & 0 \\ * & * & * & * & * & * & * \\ 0 & b_2^6 & b_3^6 & b_4^6 & b_5^6 & b_6^6 & b_7^6 \end{pmatrix}$$

The rows with $*$'s are the unconstrained rows and the b_j^i are the bspline derivatives. Now to choose a set of null vectors X_j such that,

$$m' X_j = 0 \tag{18}$$

15

Let us choose

$$X_j = \begin{pmatrix} 0 & 0 & 0 \\ 1 & 0 & 0 \\ x_{11} & 0 & 0 \\ 0 & 1 & 0 \\ x_{12} & x_{21} & 0 \\ 0 & 0 & 1 \\ x_{13} & x_{22} & x_{31} \end{pmatrix}$$

So we can compute the null vectors using equation 18.

Now the mass matrix **M** is modified by using the null vectors for linear combinations as,

$$row_2 = row_2(original) + x_{11} * row_3 + x_{12} * row_5 + x_{13} * row_7$$

$$row_4 = row_4(original) + x_{21} * row_5 + x_{22} * row_7$$

$$row_6 = row_6(original) + x_{31} * row_7$$

This has to be done for all values of the azimuthal wave number m.

This procedure can similarly be applied to all the flow vectors and scalars appearing in the vector f. The derivation of constraints is similar for higher order splines.

CFL and Modal Reduction

Another concern arising due to a cylindrical mesh is that near the origin the aspect ratio of the cells gets very high, so we have to reduce the number of azimuthal modes near the origin to maintain a good CFL number. This we will call mode suppression. So we effectively reduce the number of azimuthal modes to 1 near the origin and increase it successively such that at the outer boundary we have all the azimuthal modes.

This reduces the accuracy but helps us increase the time-step, dt, by a significant amount. Another advantage of doing this is that the computational domain in Fourier space is significantly smaller thus allowing faster computations. $i.e.$ For lower azimuthal wave number x, the computations have to carried out for more radial points, but as x increases fewer radial points have to be considered. Another way to look at it would be near the origin fewer x loops need to be considered.

16

This is to be implemented by making the upper bound of the x-loops to be dependent on y, *i.e.* $x = 1$ to nx-modified[y] if the y-loop is the outer loop, or making the lower bound of the y-loop dependent on x if the x-loop is the outer loop, *i.e.* $y = $ ny-min[x] to ny.

Optimizations

The code was optimized thus,

- Moved all major computations (rhs of governing equations) to separate subroutines thus reducing the load on the main program and enabling it to be unrolled and vectorized more efficiently.

- Manually unrolled the quadrature sum loops. This helped in decreasing the number of operations by eliminating a lot of repetitive computations due to proper regrouping. Similar and symmetric matrix multipliers were regrouped together thus reducing redundant calculations.

- Vectorizing over larger loops.

Following the above procedure has helped reduce the time taken per mode per Runge-Kutta step considerably.

Boundary conditions

Ideally, the computational domain should mimic the physical domain by including all free space and only having physical boundaries. But this is not possible and the computational domain has to be finite. So we need artificial boundaries to limit the computational domain. But we want these artificial boundaries to be invisible to the flow field so that vortices and other waves can pass through these boundaries and leave the domain without giving rise to spurious reflection waves. So we need non-reflecting boundary conditions (NRBCs).

In solving a temporally evolving jet the inflow-outflow boundaries are made periodic (see fig 2). This might not be very accurate but serves the purpose of studying turbulence. Also it takes care of the inflow-outflow boundary conditions. This also enables us to use a spectral expansion in the axial direction. So the only boundaries of concern are the

transverse numerical boundaries. If we have good boundary conditions we can make the computational domain smaller and thus get a higher resolution and compute finer scales.

Several investigators [9-14] have studied and used different types of non-reflecting boundary condtions. Engquist and Majda [12,13] study the wave equation and develop a perfectly non-reflecting boundary condition using pseudo-differential operators. But this equation is non-local in both space and time and is of little use for computational purposes as we would have to store data on the boundary from previous time-steps. But by approximating the operator they also develop a hierarchy of approximate NRBCs , with the increasing accuracy in passing obliquely incident waves.

We use the first order non-reflecting boundary conditions for outflow at the transverse boundary, which can also be derived from physical considerations using 1-D Riemann Invariants. The outflow boundary condition is,

$$\frac{\partial}{\partial t}p' - \rho_\infty c_\infty \frac{\partial}{\partial t}u'_r = -\frac{c_\infty}{2\,R}p' \tag{19}$$

where R is radius of outer boundary, and the primed quantities represent the perturbations from mean flow and the ∞ quantities represent free stream or mean flow. The term on the right hand side is a correction for a cylindrical boundary.

This boundary condition is supposed to ensure that there are no incoming waves from infinity. It works well for directly incident waves. We think that this will serve the purpose since we would have nearly cylindrical wavefronts incident on the boundary which is also cylindrical. In addition we hope to mitigate the outgoing wave amplitudes by coarsening the mesh gradually as we approach the boundary as was done in the 2-D preliminary work.

Now to implement this boundary condition in our scheme we have to transform the last set of equations, which represent the physics at the boundary, to characteristic variables at each substep of the Runge-Kutta algorithm.

This is done using the following transformation matrix from Giles.[9]

18

$$\begin{pmatrix} c_1 \\ c_2 \\ c_3 \\ c_4 \\ c_5 \end{pmatrix} = \begin{pmatrix} \rho_\infty^2 c_\infty^2 & 0 & 0 & 0 & 1 \\ \rho_\infty^2 c_\infty u_\theta & c_\infty & 0 & 0 & 0 \\ -\rho_\infty^2 c_\infty u_r & 0 & -c_\infty & 0 & 1 \\ \rho_\infty^2 c_\infty u_z & 0 & 0 & c_\infty & 0 \\ \rho_\infty^2 c_\infty u_r & 0 & c_\infty & 0 & 1 \end{pmatrix} \begin{pmatrix} \delta\sigma \\ \delta m_\theta \\ \delta m_r \\ \delta m_z \\ \delta p \end{pmatrix} \tag{20}$$

where the c_i's are the characteristic variables and the δ-quantities are time incremental quantities.

So we can modify the last five rows of the mass matrix and the right-hand-side using the above transformation.

Equation 19 can be written as

$$-\rho_\infty^2 c_\infty u_r \delta\sigma - c_\infty \delta m_r + \delta p = -\frac{c_\infty}{2\,R} p' \tag{21}$$

So to implement the above b.c. we have to replace the third of the last five rows including the right-hand-side by the above equation since the third characteristic c_3 has the right form for the b.c.

19

Test Case : Spherically Radiating Flow in a Cylindrical Domain

A few simple test cases were run to validate the code and for diagnostic purposes. In all cases the desired steady state solutions were obtained to machine accuracy. Here we present a case to test the non-reflecting b.c's.
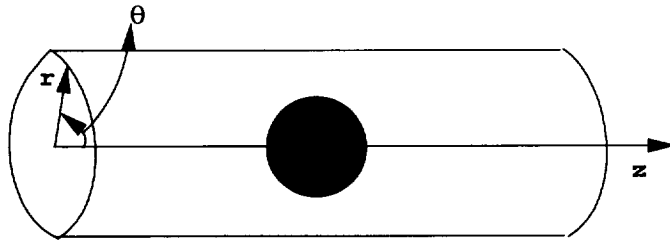
Fig. 3

We consider a spherically radiating point source flow placed at the center of a cylindrical domain. The solution is singular at the origin and is therefore picked up after a finite time and is treated as an initial value problem. This test case is very robust, since there exists an exact time-dependent solution with which we can compare our results. This test case not only tests the non-reflecting boundary conditions but also validates the entire code.

The radiating bubble is considered as a perturbation to the mean flow which is,

$P = \frac{1}{\gamma}$, $\sigma = 1$, $u_r = u_z = u_\theta = 0$

The perturbation is taken as a point source solution of the linear wave equation which is written as a velocity potential $\Phi(t - \frac{x}{c})$. Where $x = \sqrt{r^2 + z^2}$, c is sound speed, and t is the time. Φ can be any function.

We have used a cubic function(a gaussian function has also been tried) for Φ,

20

$$\Phi = \begin{cases} -\frac{1}{4\pi x}(t - \frac{x}{c})^3(t_1 - t + \frac{x}{c})^3, & c(t - t_1) < x < ct \\ 0 & otherwise \end{cases}$$
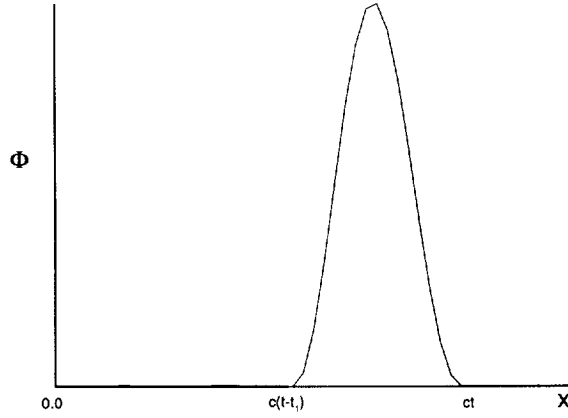
The function is plotted below.

Fig. 4

The fundemental perturbations are expressed in terms of the velocity potential as,

$$p' = -\rho_\infty \frac{\partial \Phi}{\partial t}$$

$$\sigma' = -p'$$

$$u'_r = \frac{\partial \Phi}{\partial r}$$

$$u'_\theta = 0.$$

$$u'_z = \frac{\partial \Phi}{\partial z}$$

Plotted below are the density profiles as time progresses. The dotted profiles which almost overlap the solid lines are the exact solutions. From the plots we can see that the non-reflecting conditions work fairly well. The waves which are incident normally pass through the artificial boundaries with little or no reflection. In figures 5 and 7 the plots with $t = t_3$ show a weak reflected residual wave. This is as expected since the non-reflecting conditions are exact for normally incident waves, but oblique waves would cause some reflection.

21

A more general test case was done by shifting the origin of the point source off the z-axis. So the flow is not symmetric anymore and u'_θ is not zero. This allows more azimuthal modes and also the the waves reaching the boundary are not normal incident anymore. This also validates the flow solver. Figure 8 shows very minimal reflection for the off-centered test case.
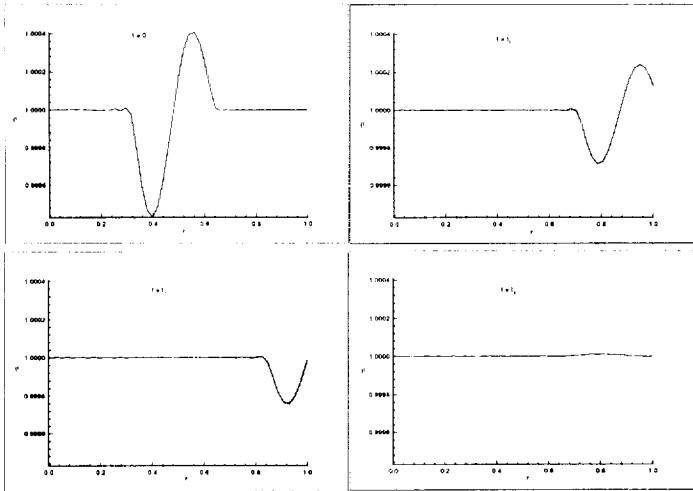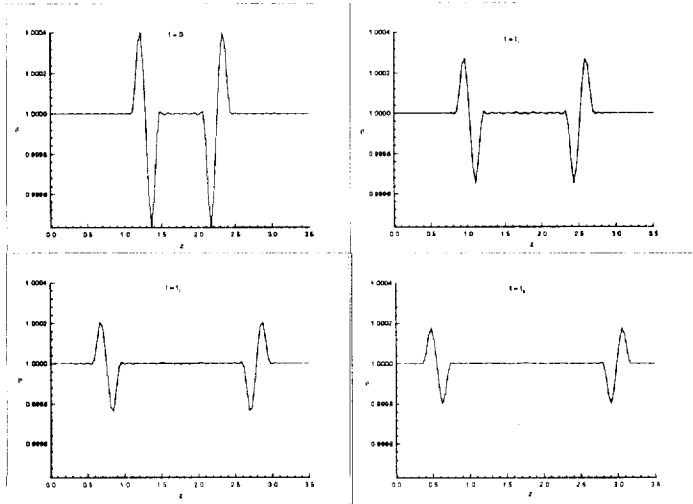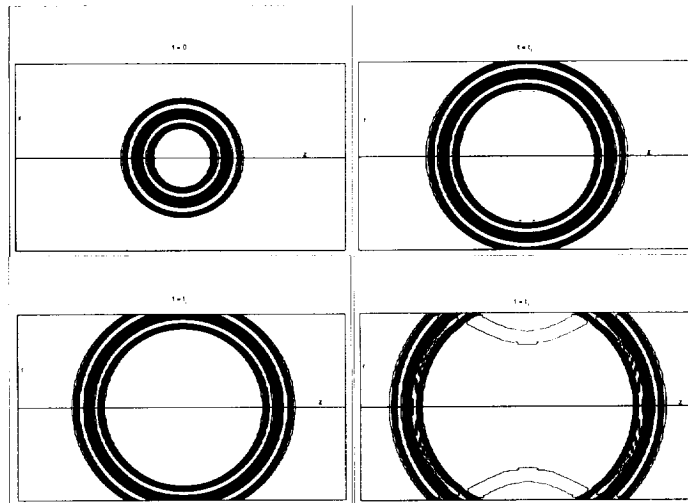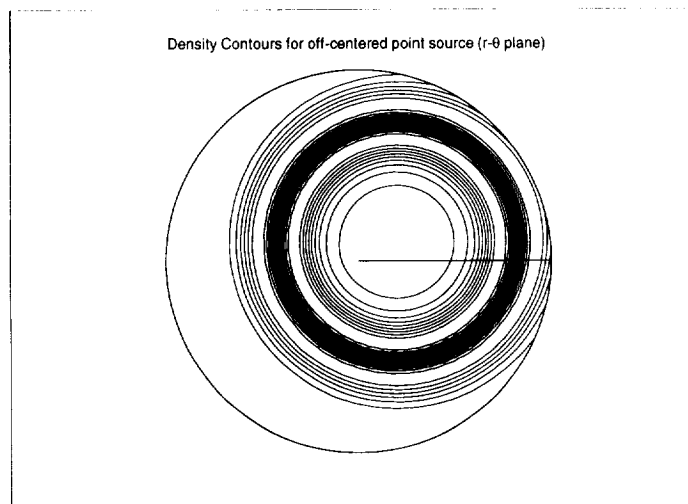

Fig. 5

Fig. 6

Fig. 7

Density Contours for off-centered point source (r-θ plane)

Fig. 8

Preliminary Results for M = 2 Jet

A preliminary computation with a coarse mesh (64*67*32) was done for M = 2 jet. The initial conditions were taken to be a "half-Gaussian" velocity profile super-imposed with a combination of the most unstable eigenfunctions of the stablility problem. We have a single helical mode with $k_\theta = 4$ and $k_z = 3$. This makes the jet length to be about 2.1 times the jet radius. The Reynolds number based on the jet radius and velocity of sound for this simulation is 2500.

Since we use instabilities in the azimuthal direction which have a wave number of 4 the ensuing flow will have structures which are multiples of 4. So the quarter domain problem can be solved, since there is quadrant symmetry. This was verified in the preliminary run to ensure the validity of the code.

Below are presented the results of a quarter domain simulation on a relatively coarse mesh (32*67*84). So that is 32 modes in the azimuthal direction but over a quarter domain. The Jet unperturbed velocity is M = 2. The Re is still 2500. The simulation was stopped when undamped delta waves begin to grow. At present we are working on a filter to remove these spurious waves.

The energy spectrum is plotted versus the axial and the azimuthal wave numbers. The plots show a wide spectrum of energy. The initial conditions had energy only in the $k_z = 1$ and $k_\theta = 1$ modes. This indicates that the energy has been cascaded to other modes as the jet developed. So as expected a wide range of scales can be observed. The solid line shown is the $k^{-5/3}$ spectrum. So we get a decade of $k^{-5/3}$ spectrum. Better resolution gives us better agreement with the $k^{-5/3}$ spectrum.

Figure 11, below shows the growth in the mean thickness of the shear layer at different times of the simulation. We observe a four-fold increase in the shear layer thickness from initial to the final time at which the simulation was stopped.

Shown in figures 12 and 13 are cross-sectional plots of the three components of velocity,vorticity and the pressure and density at the final time (t = 6.564). The formation of spiral structures is also visible. A flow that was initially laminar develops turbulent structures. A higher resolution simulation would help capture the smaller scales better.
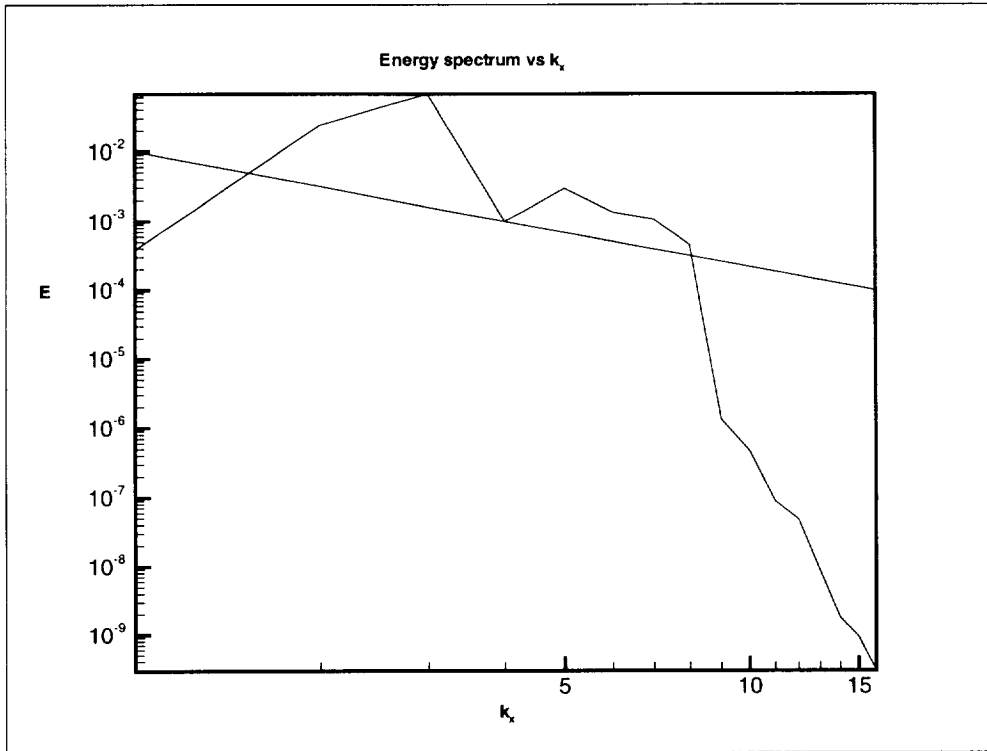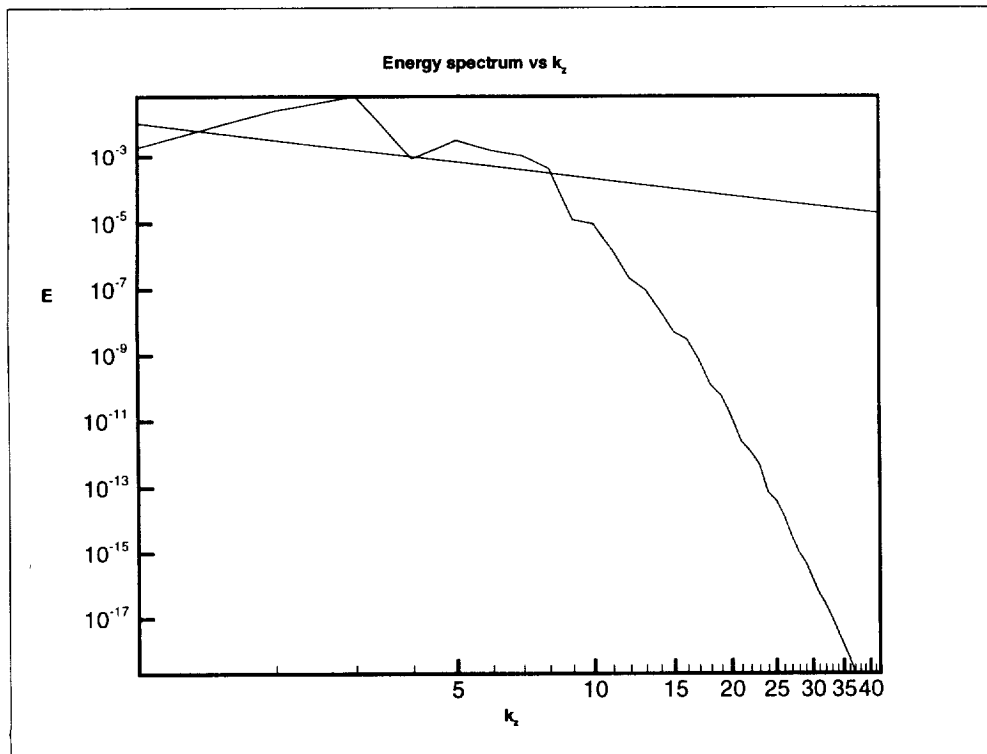
Fig. 9 : Plots showing the energy spectrum vs k_θ

Fig. 10 : Plot showing the energy spectrum vs k_z
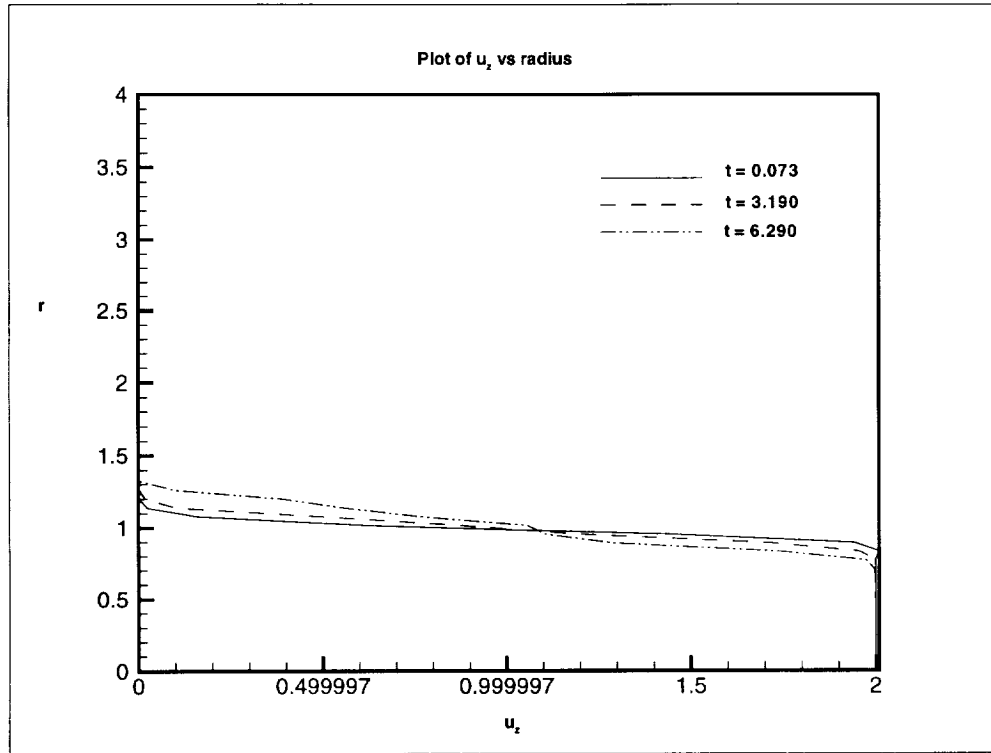
25

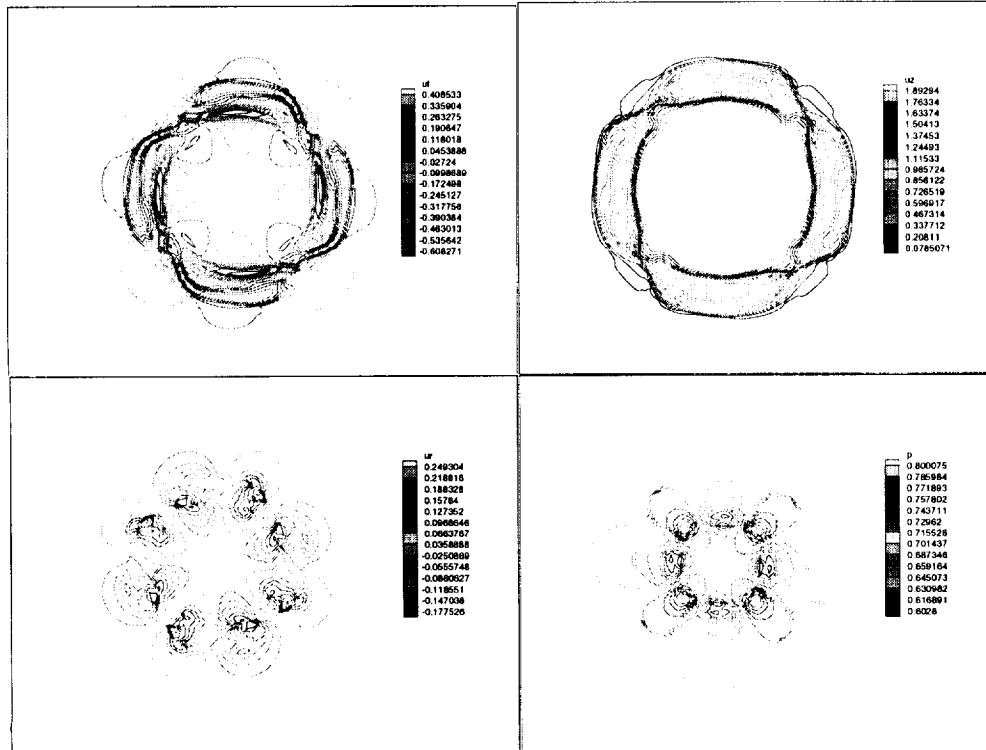Fig. 11 : Plot showing the growth of shear layer thickness over time

Fig. 12 : $r - \theta$ cross-sectional plots of velocity components and pressure
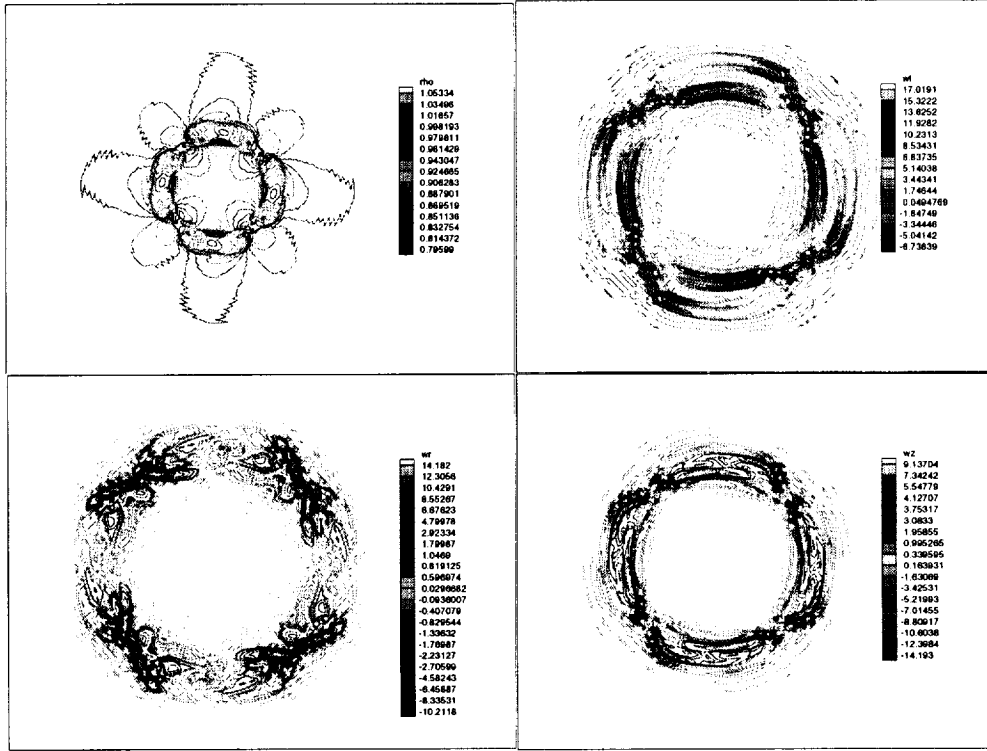
26

Fig. 13 : $r - \theta$ cross-sectional plots of density and vorticity components

Shown below is a reconstruction of the jet by placing adjacent to each other flow solutions at different times. The phase velocity was taken to be the velocity with which the disturbances traverse the domain in the axial direction. So the plots adjacent are taken at time intervals equal to the time it takes the disturbances to travel the domain length. We do see some discontinuity at the zonal boundaries since they are not exactly at the time intervals desired. But the picture looks good enough for us to conclude that such a reconstruction could be used not only to see the jet structure and growth but also to compute the near field acoustic signature. The flow quantity plotted is the total vorticity magnitude. It is evident from the plot that the initially sharp shear layer grows thicker and has a more varied structure showing the growth and development of helical vortices.

Plotted above the jet is the total pressure energy $(p * u_r)$ (or the energy outflux) radiated through a cylindrical shell , chosen to be r = 3 in this case. This gives a rough estimate of when acoustic energy was radiated. From the plot we see that there is a sharp rise in the energy flux after t = 2. This is when the initial disturbances in the shear layer

propogate to r = 3. Also around t = 4 there is another fluctuation which is due the growth and non-linear interactions. The energy outflux increases as we proceed in time indicating that acoustic emissions are now due to the tubulent behavior of the jet. There is growth of helical vortices. We also expect to some sharp fluctuations in the plot when the breakdown of the helical vortices occurs. So a direct correlation can be drawn between the flowfield and the affected energy flux. Bearing in mind that what happens at the shear layer (r = 1) takes another 2 units of time to reach the location r = 3 at which the energy flux is computed.

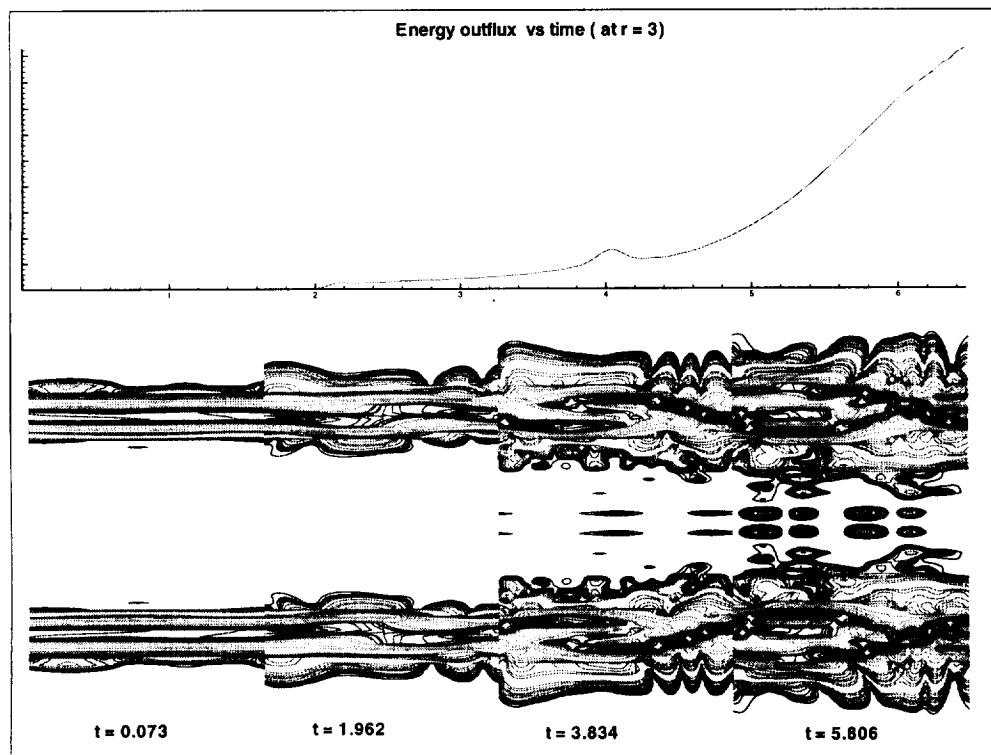Fig. 14 : Vorticity magnitude at different times and the total energy flux associated with this flow

References for Chapter 2

[1] De Boor, C., " *A Practical Guide to Splines* ", Springer-Verlag, 1978.

[2] Tam, C. K. W., and Burton, D. E., "Sound Generated by Instability Waves of Supersonic Jets, Part 1. Two Dimensional Mixing Layers, Part 2. Axissymmetric Jets", *J. Fluid Mech.*, **138**, 1984, pp.249 -271, 273-295.

[3] Tam, C. K. W., " Stochastic Model Theory of Broadband Shock Associated Noise from Supersonic Jets", *Journal of Sound and Vibration*, **116**, 1987, pp.265-302.

[4] Tam, C. K. W., and Tanna, H. K., " Shock Associated Noise from Supersonic Jets from Convergent-Divergent Nozzles", *Journal of Sound and Vibration*, **81**, 1982, pp.337-358.

[5] Gardner, L. R. T., Gardner, G. A., Zaki, S. I., and El Sahhrawi, Z., " B-Spline Finite Element Studies of the Non-Linear Schrodinger Equation". *Computer Methods in Applied Mechanics and Engineering*, **108**, September 1993, pp.303-318.

[6] Kasi Vishwanadham, K. N. S., and Koneru, S. R., " Finite Element Method for One-Dimensional and Two-Dimensional Time Dependent Problems with B-Splines", *Computer Methods in Applied Mechanics and Engineering*, **108**, September 1993, pp.201-222.

[7] Moser, R. D., Moin, P., and Leonard, A., " A Spectral Numerical Method for the Navier-Stokes Equations with Applications to Taylor–Couette Flow ", *J. Comp. Phys.*, **52**, No. 3, December 1983, pp.524-544.

[8] Shariff, K., " Comment on Coordinate Singularities by P. R. Spalart ", Personal Communication.

[9] Giles, M. B., " Non-reflecting Boundary Conditions for Euler Equation Calculations", AIAA *Journal*, **28**, December 1990, pp.2050-2058.

[10] Colonious, T., Lele, S. K., Moin, P., " Boundary Conditions for Direct Computations of Aerodynamic Sound Generation", AIAA *Journal*, **31**, No.9, September 1993, pp.1574-1582.

[11] Poinsot, T. J., and Lele, S. K., " Boundary Conditions for Direct Simulations of

Compressible Viscous Flows ", *J. Comp. Phys.*, **101**(1), 1992, pp. 104-129.

[12] Engquist, B., and Majda, A., " Absorbing Boundary Conditions for the Numerical Simulation of Waves ", *Math. Comput.*, **31**(139), 1977, pp. 629-651.

[13] Engquist, B., and Majda, A., " Radiation Boundary Conditions for Acoustic and Elastic Wave Calculations ", *Commun. Pure Appl. Math.*, **32**, 1979, pp. 313-357.

[14] Givoli, D., " Non-Reflecting Boundary Conditions ", *J. Comp. Phys.*, **94**, 1991, pp. 1-29.

[15] Sandham, N. D., and Reynolds, W. C., " Compressible Mixing Layer : Linear Theory and Direct Simulation ", AIAA *Journal*, **28**, 1989, pp.618 - 624.

[16] Sandham, N. D., and Reynolds, W. C., " Three-Dimensional Simulation of Large Eddies in the Compressible Mixing Layer ", *J. Fluid Mech.*, **224**, 1991, pp.133-158.

Appendix

The compressible Navier-Stokes equations in cylindrical coordinates

$$\frac{\partial \rho}{\partial t} + \frac{1}{r}\frac{\partial (r\rho u_r)}{\partial r} + \frac{1}{r}\frac{\partial (\rho u_\theta)}{\partial \theta} + \frac{\partial (\rho u_z)}{\partial z} = 0 \qquad (A.1)$$

$$\rho\left(\frac{Du_r}{Dt} - \frac{u_\theta^2}{r}\right) = -\frac{\partial P}{\partial r} + \frac{\partial \tau_{rr}}{\partial r} + \frac{1}{r}\frac{\partial \tau_{r\theta}}{\partial \theta} + \frac{\partial \tau_{rz}}{\partial z} + \frac{\tau_{rr} - \tau_{\theta\theta}}{r}$$

$$\rho\left(\frac{Du_\theta}{Dt} + \frac{u_r u_\theta}{r}\right) = -\frac{1}{r}\frac{\partial P}{\partial \theta} + \frac{\partial \tau_{\theta r}}{\partial r} + \frac{1}{r}\frac{\partial \tau_{\theta\theta}}{\partial \theta} + \frac{\partial \tau_{\theta z}}{\partial z} + 2\frac{\tau_{r\theta}}{r} \qquad (A.2)$$

$$\rho\frac{Du_z}{Dt} = -\frac{\partial P}{\partial z} + \frac{\partial \tau_{zr}}{\partial r} + \frac{1}{r}\frac{\partial \tau_{z\theta}}{\partial \theta} + \frac{\partial \tau_{zz}}{\partial z} + \frac{\tau_{zr}}{r}$$

where,

$$\tau = \mu \begin{pmatrix} 2\left(\frac{\partial u_r}{\partial r} - \frac{1}{3}\nabla \cdot \vec{u}\right) & \frac{1}{r}\frac{\partial u_r}{\partial \theta} + r\frac{\partial}{\partial r}\left(\frac{u_\theta}{r}\right) & \frac{\partial u_z}{\partial r} + \frac{\partial u_r}{\partial z} \\ \frac{1}{r}\frac{\partial u_r}{\partial \theta} + r\frac{\partial}{\partial r}\left(\frac{u_\theta}{r}\right) & 2\left(\frac{1}{r}\frac{\partial u_\theta}{\partial \theta} + \frac{u_r}{r} - \frac{1}{3}\nabla \cdot \vec{u}\right) & \frac{\partial u_\theta}{\partial z} + \frac{1}{r}\frac{\partial u_z}{\partial \theta} \\ \frac{\partial u_z}{\partial r} + \frac{\partial u_r}{\partial z} & \frac{\partial u_\theta}{\partial z} + \frac{1}{r}\frac{\partial u_z}{\partial \theta} & 2\left(\frac{\partial u_z}{\partial z} - \frac{1}{3}\nabla \cdot \vec{u}\right) \end{pmatrix}$$

$$\frac{D}{Dt} = \frac{\partial}{\partial t} + u_r\frac{\partial}{\partial r} + \frac{u_\theta}{r}\frac{\partial}{\partial \theta} + u_z\frac{\partial}{\partial z}$$

$$\nabla \cdot \vec{u} = \frac{1}{r}\frac{\partial r u_r}{\partial r} + \frac{1}{r}\frac{\partial u_\theta}{\partial \theta} + \frac{\partial u_z}{\partial z}$$

μ is the viscosity,

$$\frac{\partial P}{\partial t} + \nabla \cdot P\vec{u} = -(\gamma - 1)P\nabla \cdot \vec{u} + (\gamma - 1)\nabla \cdot \vec{q} + (\gamma - 1)\Phi \qquad (A.3)$$

$\vec{q}$ is the heat flux, T is the temperature, κ is heat conductivity,

$$\vec{q} = -\kappa \nabla T, \qquad T = \gamma\, \sigma\, P$$

and Φ is viscous dissipation given by,

$$\Phi = \mu\left(2\left(\left(\frac{\partial u_r}{\partial r}\right)^2 + \left(\frac{1}{r}\frac{\partial u_\theta}{\partial \theta} + \frac{u_r}{r}\right)^2 + \left(\frac{\partial u_z}{\partial z}\right)^2\right)\right.$$
$$\left. + \left(\frac{1}{r}\frac{\partial u_z}{\partial \theta} + \frac{\partial u_\theta}{\partial z}\right)^2 + \left(\frac{\partial u_r}{\partial z} + \frac{\partial u_z}{\partial r}\right)^2 + \left(\frac{1}{r}\frac{\partial u_r}{\partial \theta} + \frac{\partial u_\theta}{\partial r} - \frac{u_\theta}{r}\right)^2 - \frac{2}{3}(\nabla \cdot \vec{u})^2\right)$$

Acknowledgements